# Origin of the high conductivity anomalies in the mid-lower crust of the Tibetan Plateau: Dehydration melting of garnet amphibolites

Xinzhuan Guo[1,*], Sibo Chen[2, 3], Chao Zhang[2], Yao Wu[2], Wang Xiong[2], Yanfei Zhang[2], Xiang Wu[2], Junfeng Zhang[2]

[1]Key Laboratory for High-Temperature and High-Pressure Study of the Earth's Interior, Institute of Geochemistry, Chinese Academy of Sciences, Guiyang 550081, China

[2]State Key Laboratory of Geological Processes and Mineral Resources, China University of Geosciences, 430074 Wuhan, China

[3]Department of Geosciences, Stony Brook University, Stony Brook, New York 11794–2100, USA

[*]Corresponding author: Xinzhuan Guo (gxzhuan@mail.gyig.ac.cn)

**Key Points:**

- Amphibole dehydration at 1100 K and 1.5 GPa induces partial melting of amphibolites
- Dehydration melting of amphibolite contributes to the high EC anomalies in Tibetan Plateau
- The estimated melt volume fractions of the partial molten region are 3.8–36 vol%

## Abstract

High-conductivity anomalies of 0.1–1 S/m are widely distributed in the mid-lower crust of the Tibetan Plateau. Dehydration of amphibole-bearing rocks may play an important role in explaining these anomalies. To survey the anomalies' origin, therefore, the electrical conductivities of amphibole-bearing samples, containing varying amphibole content, are measured at 1.5 GPa and 600–1300 K. Our experiments show that dehydration melting occurs at about 1100 K. Proton conduction and ionic conduction dominate the conduction mechanisms before and after dehydration melting, respectively. The dehydration melting of felsic rocks, containing 25 vol% of amphibole, is unable to account for the high-conductivity anomalies of 0.1–1 S/m. In contrast, the dehydration melting of garnet amphibolite, with an amphibole content higher than 60 wt%, can enhance the bulk conductivity to higher than 0.1 S/m under the lower-crust conditions beneath the Tibetan Plateau. The melt fraction of the garnet-amphibolite is estimated to be 3.8–36 vol% in the partial molten region based on a cube-model simulation.


## Plain Language Summary

The origin of high-conductivity anomalies within the mid-lower crust of the Tibetan Platear is a long-standing controversial issue. High conductive phases, including brine-bearing aqueous fluids, melts, graphite, and metal sulfides, have been proposed to be present in this region to explain the high conductivity anomalies. In view of the high surface heat flow, especially, in the southern Tibetan Plateau, partial melting likely prevail in the lower crustal condition. In this study, we conducted a series of high-temperature and high-pressure experiments and in-situ measured the electrical conductivity of garnet-amphibolites (main rock type in this region) with different contents of amphibole. Our experiments show that dehydration melting of garnet amphibolite can

contribute the conductivity comparable to the high conductivity anomalies. The melt fraction of garnet-amphibolites was determined to be higher than 3.8 vol% in the partial molten region based on a geometric model.

**Key words:** Electrical conductivity, amphibolite, dehydration melting, high-conductivity anomalies, Tibetan Plateau, crust

## 1 Introduction

Geophysical observations have confirmed that high-conductivity layers (0.1–1 S/m) are widely distributed in the mid-lower crust of the Tibetan Plateau (Nelson et al., 1996; Wei et al., 2001; Unsworth et al., 2005; Le Pape et al., 2012). These high-conductivity layers are usually combined with the feature of low velocity (Shapiro et al., 2004; Hacker et al., 2014). Many experiments have been conducted to establish the origin of these low-velocity–high-conductivity zones (LV-HCZs) within the Tibetan crust. Nevertheless, the possible origin is a long-standing and controversial issue. Electrical conductivities of typical crustal rocks, such as granulite (Fuji-ta et al., 2004), gabbro (Kariya & Shankland 1983), quartzite (Shimojuku et al., 2012), and granite (Olhoeft, 1981), have been proved to be much lower than the high-conductivity anomalies. Furthermore, the electrical conductivity of hydrous “clinopyroxene + plagioclase” model is high enough to explain the high-conductivity anomalies in the Tibetan Plateau (Yang & Keppler, 2012). Therefore, high-conductivity materials with good connectivity are expected to exist in these LV-HCZs. Metallic minerals, such as iron and copper sulphide, and graphite films can be easily ruled out due to the limited spatial distribution and low stability at geological time-scales (Yoshino & Noritake, 2011).

Aqueous fluids and melts are characterized by high conductivity, which can reduce the velocity in solid rock. Therefore, LV-HCZs within the mid-lower crust of the Tibetan Plateau are usually comprised of partial melts, either mantle-derived (Roger et al., 2000; Tapponnier et al., 2001) or crustal-derived partial melts (Wang et al., 2016), or aqueous fluids (Makovsky & Klemperer 1999), or a combination of aqueous fluids and partial melts (Li et al., 2003). Previous experimental studies have shown that small amounts of NaCl solution can strongly enhance the bulk conductivity to the geophysically observed conductivity anomalies (Guo et al., 2015). However, a brine-bearing, crustal-rock model is only applicable in regions with a low geotherm. The mid-lower crust of the Tibetan Plateau has undergone amphibolite-to-granulite-facies regional metamorphism and anatectic melting (Zhang et al., 2015). A partial melting model is likely to prevail with the aid of released water from hydrous minerals. Deep crustal xenoliths in the Tibetan Plateau indicate that amphibolites, and garnet amphibolite in particular, are important rock types in the lower crust of Tibet (Hou et al., 2017; Kang et al., 2019). Sufficiently abundant regionally aligned lattice orientation of amphibole in these rocks may be the principal contributor to the seismic anisotropy (Ozacar & Zandt, 2004; Ji et al., 2015; Tatham et al., 2008). Partial dehydration melting of amphibolite and garnet amphibolite under lower crustal conditions is a potential candidate model for explaining seismic anisotropy and is also the origin of LV-HCZs in the mid-lower crust of the Tibetan Plateau. However, it has not been experimentally examined.

In the present study, we measured the electrical conductivity of amphibole-bearing samples, containing varying contents of amphibole, at 1.5 GPa and 600–1300 K. Our experiments show that the dehydration of garnet amphibolite can enhance its bulk conductivity to values comparable to those of high-conductivity anomalies in the mid-lower crust of the Tibetan Plateau, and calibration shows that melt fraction of 3.8% and 36% can account for the high conductivity anomalies of 0.1

and 1 S/m, therefore, presenting a new model to explain the origin of these high-conductivity anomalies in the mid-lower crust of the Tibetan Plateau.

## 2 Experimental Methods

Four types of samples, Amp25-Pl, Amp100, Grt-Amp80 and Grt-Amp60, are used as the starting materials for the electrical conductivity measurements. A fresh natural amphibole-plagioclase gneiss (D17T87, collected from Qushui within the Lhasa block), consisting of plagioclase (55 vol%), quartz (10 vol%), amphibole (25 vol%), clinopyroxene (5 vol%), and accessory minerals (5 vol%, including ilmenite, zircon, and rutile), was ground into a fine powder with a grain size of less than 20 μm. The powder mixture was hot-pressed in an unsealed Mo capsule at 1.5 GPa at 873 K for 24 h using a piston cylinder press to prepare an Amp25-Pl sample. Another natural garnet amphibolite sample (16LZWX2, collected from the eastern Himalayan syntaxis) was used to prepare samples of Amp100, Grt-Amp80, and Grt-Amp60. Garnet and amphibole grains were separated from it using a vibrating sifter and were further ground into powders with a grain size of less than 20 μm. All powders were baked at 393 K in a vacuum stove before being hot-pressed to extract moisture absorbed from the air. Then, the carefully prepared powders of amphibole (100 wt%), garnet-(20 wt%)-amphibole-(80 wt%), and garnet-(40 wt%)-amphibole-(60 wt%) were individually hot-pressed at 1.5 GPa at 873 K for 24 h. The sintering process, without detectable phase changes checked by scanning electron microscope (SEM), made the sample machinable and more dense. All hot-pressed samples were then shaped into cylinders 2 mm in diameter and 1 mm in length by an ultrasonic drilling machine.

A Walker-type Rockland 1000-ton apparatus installed at the State Key Laboratory of Geological Processes and Mineral Resources, China University of Geosciences, was used in the high-temperature and high-pressure experiments. Eight WC anvils, each with a truncated edge

length of 15 mm, were used as second-stage anvils. A $Cr_2O_3$-doped MgO octahedron with an edge length of 25 mm was used as the pressure medium. A detailed cell design has been discussed elsewhere (Li et al., 2018). The difference is that we used a BN capsule rather than a single-crystal quartz capsule in this study. The objective of this work is to assess the effect of the dehydration melting of an amphibole-bearing sample on its bulk conductivity. To avoid water escaping from the cell assembly, conductivity measurements should be conducted in a closed system, in principle. However, this is impractical because of the difficulty in sealing in water using an insulating material. Despite a single-crystal quartz together with a thick-disk Au electrode can provide a closed environment, the quartz capsule is not in chemical equilibrium with the sample. As a result, a hexagonal BN capsule was used instead in this study. We should note that the use of BN capsule in the experiment will cause weight percent level of boron to incorporate into the hydrous melt and part of water may escape during the high P-T conductivity measurements.

Electrical conductivity measurements were performed using a Solartron 1260 impedance gain-phase analyzer, operating at a 1 V amplitude alternating current and at frequencies of $10^6$–$10^{-1}$ Hz. Electrical conductivities of the samples were obtained using the equation $\sigma=l/(s\cdot R)$, where $l$, $s$, and $R$ denote sample length (m), sample section area ($m^2$), and sample resistance (Ω), respectively. A typical conductivity measurement of the Grt-Amp sample was performed as follows: The sample was pressurized to 1.5 GPa at room temperature. The sample was then heated from 600 or 700 K to 1300 K in 50 K intervals. If dehydration melting occurs, the bulk conductivity strongly increases due to fluid effects (Chen et al., 2018; Manthilake et al., 2015). Sample conductivity, therefore, was measured at least twice at each temperature, with a 10-minute interval, to monitor the onset of dehydration. The conductivities were measured from 1300 to 600 K in 50 K intervals. Then, the sample was re-heated to 1300 K and kept at that temperature for 1 or 2 h.

131 Finally, the sample was quenched by cutting off the power supply to preserve the sample texture
132 at a high temperature.

133 The textures of the recovered samples were observed using a Quanta2000 scanning electron
134 microscope (FE-SEM); and the chemical compositions of each phase were analyzed using a JXA-
135 8100 electron microprobe with an accelerating voltage of 15 kV, a beam current of 20 nA, and a
136 beam size of 1–5 μm for mineral analysis. The melt fraction was estimated by counting the area
137 fraction of the melts of the recovered samples using Image-J software. For melt analysis, the beam
138 current and beam size were 10 nA and 7–10 μm, respectively.
139

140 **3 Experimental Results**

141 Figure 1 shows the electrical conductivity of the Amp25-Pl sample as a function of time
142 (minute). The conductivity became stable after sintering of the sample at 900 K for 40 minutes
143 (R1040). This process can efficiently eliminate the effect of absorbed moisture on conductivity
144 measurements. When the temperature was increased to 1100 K, the conductivity increased slowly
145 and continuously at each experimental temperature. This indicates the onset of dehydration melting
146 of the sample; however, the dehydration effect on conductivity in the sample is much weaker than
147 that in phengite (Chen et al., 2018). The slow increase in conductivity after the onset of dehydration
148 melting is possibly due to the fact that the hydrous melt in this study contains more viscous boron
149 component, which reduces the mobility of electrical charge carriers in the melt. To achieve texture
150 equilibrium, we increased the temperature to, and maintained it at, 1300 K for 12 h. The electrical
151 conductivity decreased by 0.15 S/m during this sintering process. In another two experiments
152 (R1055, R1056), we sintered the samples at 1250 K and 1200 K for 12 h, respectively, and then

acquired the impedance spectra of the samples. The logarithmic conductivity of Amp25-Pl samples at 1300 K is highest, but it is just 0.1 S/m higher than that at 1200 K (Table 1).

Three experiments on the garnet-amphibolite system, containing 100, 80, and 60 wt% amphibole were performed at temperatures of up to 1300 K at 1.5 GPa. Figure 2 shows the electrical conductivity of Amp100 as a function of reciprocal temperature. We acquired the impedance spectra during several heating-cooling cycles. The data are very consistent before heating the sample to 1000 K. There was no abrupt change in electrical conductivity until 1300 K despite previous phase equilibrium experiments showing that the dehydration melting of garnet amphibolite occurs at 1123 K at 1.5 GPa (Wang et al., 2019; Ye et al., 2021). During cooling of the sample from 1300 K to 950 K, its logarithmic conductivity decreased linearly with increasing reciprocal temperature. The relationship between the sample's electrical conductivity and its temperature can be expressed by the Arrhenius formula:

$$\sigma_{bulk} = \sigma_0 \exp(-\Delta H / kT) \qquad (1)$$

where $\sigma_0$ is the pre-exponential factor (S/m), $\Delta H$ is the activation enthalpy (eV), $k$ is the Boltzmann constant (J/K), and $T$ is the absolute temperature (K). The activation enthalpy dramatically decreased from 0.85 at 1300–950 K to 0.055 eV at 900–600 K. The distinctive low activation enthalpy at 900–600 K is attributed to the water exsolution from the melt during cooling of the sample. The electrical conductivities in the final heating path were slightly lower than those obtained in the previous cooling path, indicating only small amount of water escaped from the cell assembly.

For the Grt-Amp80 sample, there was no conductivity jump due to the dehydration melting of the amphibole during heating of the sample. In the following cooling path from 1300 K, there are two distinct activation enthalpies (see the supporting information Figure S1). The change in

slope may correspond to crystallization (Yoshino et al., 2010) together with the water exsolution from the melt with descending temperatures. The activation enthalpy (1.06 eV) of the garnet-amphibole sample in the high-temperature region is slightly higher than that of the polycrystalline amphibole. In contrast, the activation enthalpy (0.50 eV) in the low-temperature region is much lower than that of the polycrystalline amphibole, indicating that most of the water is stored in the sample during cooling. The conductivities of Grt-Amp60 are almost consistent with those of Grt-Amp80 for a given temperature, but the crystallization temperature of the melt is 50 K higher (see the supporting information Figure S2).

Figure 3 shows representative textures of the samples after conductivity measurements. For the Amp25-Pl sample, the run products after being annealed at 1300 K and 1.5 GPa for 12 h include garnet, clinopyroxene, ilmenite, plagioclase, and melt. Incongruent melting of amphibole (hornblende, Hbl) produces melt, clinopyroxene, and garnet, while quartz and plagioclase are progressively consumed (Figures 3a–3c).

$$\mathrm{Hbl} + \mathrm{Qtz} \rightarrow \mathrm{Melt} + \mathrm{Grt} + \mathrm{Cpx} + \mathrm{Ilm} \quad (2)$$

$$\mathrm{Hbl} + \mathrm{Pl} \rightarrow \mathrm{Melt} + \mathrm{Grt} + \mathrm{Cpx} + \mathrm{Ilm} \quad (3)$$

As a result, the quartz and amphibole are completely consumed, while the plagioclase is saved as a residual mineral. The melt distribution is heterogeneous, and most melts are limited to the rim of the sample (Figure 3c). The melt fraction varies from 6.7 vol% at 1300 K to 6.5 vol% at 1250 K, and to 5.9 vol% at 1200 K. Ilmenite occurs as inclusions in the garnet, indicating the fast growth rate of the garnet. The chemical compositions of each mineral are listed in Table 2. The melt is andesitic in composition and is rich in water (12.6–23.7wt%, $c_{\mathrm{H_2O}} = 100\% - c_{\mathrm{total}}$). The $SiO_2$ content varies from 53.54 wt% to 56.97 wt%, independent of temperature. The melt compositions are characterized by a high $Al_2O_3$ content (19.56–21.8 wt%) and low MgO (2.79–3.76 wt%) and

199 $K_2O$ (0.42–0.47 wt%) contents. Small rounded pores are observed in the melt, which should be
200 filled with water at high pressure.

201 For the Grt-Amp samples, observation of the texture of the recovered sample shows that
202 dehydration melting of amphibole produces garnet, clinopyroxene, melt, ilmenite, and quench
203 orthopyroxene (Figures 3e, 3f, 3h, and 3i).

204 $$\mathrm{Hbl} \rightarrow \mathrm{Melt} + \mathrm{Grt} + \mathrm{Cpx} + \mathrm{Il} \qquad (4)$$

205 One to two hours annealing of the sample at 1300 K and 1.5 GPa dehydrated the amphibole
206 completely. Similar to that of the Amp25-Pl sample, the melt distribution for the Grt-Amp sample
207 was heterogeneous, and the melt concentrated at the rim of the sample. The melt segregation of
208 the partial melts during short runs using multi-anvil press was probably due to the thermal gradient
209 and /or stress gradient in the furnace assemblies, which is also reported by previous study
210 (Takahashi & Scarfe, 1985). The melt fractions for Amp100, Grt-Amp80, and Grt-Amp60 were
211 52.0 vol%, 12.4 vol%, and 9.0 vol%, respectively. Melt can be divided into three types. Melt$^a$
212 existed in the rim of the sample, in which few quench phases occurred. Melt$^b$ was separated from
213 melt$^a$ by a clear boundary, and needle-like quench orthopyroxene mainly existed in melt$^b$ (Figure
214 3f) and was typically formed by the quenching of melts at high temperature. Melt$^c$ was situated far
215 from the boundary of the sample and coexisted with clinopyroxene and garnet. These melts are
216 also distinguishable by their chemical composition. Melt$^a$ had the lowest silica content (47.45
217 wt%), followed by melt$^b$ and melt$^c$ (Table 3). The silica content of melts decreases with increasing
218 annealing temperature, consistent with previous studies of the phase equilibrium experiments
219 (Qian & Hermann, 2013; Wang et al., 2019; Ye et al., 2021). The relatively low silica content in
220 this study, compared with that of the phase equilibrium experiments may be explained as the higher
221 annealing temperature used in this research. It is also found that the silica content of the melt

decreases with increasing melt fraction of the samples. The water content of melts, defined as total weight percent deficiency, yields values of 9.83–20.00 wt%. The melts in the rim of the sample has the highest water content. The estimation of water content for all the samples should be exaggerated due to the incorporation of boron into hydrous melt at high *P*-*T* conditions. For example, water content of melt of Amp100 sample can be roughly calculated to be 8.2 wt% by mass balance, given that the density of solid phase is the same as 3.5 g/cm$^3$, the density of hydrous melt is 2.8 g/cm$^3$, and that all the dehydrated water was dissolved in the melt. The calculated value of 8.2 wt% by mass balance is similar to the water content (9.83 wt%) of melt$^c$, which is far from the BN capsule, indicating that boron has diffused into the melt. Consequently, we selected the water content of melt$^c$, 9.83 wt%, for further discussing in Figure 8. As hydrogen is more active than boron in the melt. If some amount of boron was dissolved in the melt, the viscosity would increase and lower the conductivities. That is, if there is no contamination from boron, the measured bulk conductivity should be higher.

Representative impedance spectra are shown in Figure S3. The spectra contain a slightly distorted semicircle at frequencies higher than 1000 Hz followed by a small “tail” at frequencies of 1000–0.1 Hz. The semicircle represents the electrical signal of the sample, and the small “tail” represents the electrode reaction (Roberts & Tyburczy, 1991). The radius of the impedance arc decreases with increasing temperature, indicating a semi-conductor behavior of the sample. The equivalent circuit of the sample is composed of two resistance-(R)-constant-phase-element-(CPE) parallel circuits connected in series. There is no strong shrinkage of the impedance arc, even at temperatures higher than the dehydration temperature of amphibole (around 1100 K), as has been observed during the dehydration of phengite (Chen et al., 2018). The good single-arc fitting of the sample resistance at temperatures higher than 1100 K indicates that the melt and the solid phases

behave in a parallel manner, and that the electrical conductivity of the melt dominates in the bulk conductivity of the sample.

# 4 Discussion

## 4.1 Comparison with Previous Studies

In a previous study, Wang et al. (2012) reported that the electrical conductivity of amphibole-bearing rocks dramatically increases at 800 K and 0.5–1 GPa (Figure 4). They proposed that dehydration of amphibole associated with the oxidation of iron from ferrous to ferric iron contributed to this conductivity jump, rather than the released free fluid. The activation enthalpy was strongly enhanced from 0.66–0.69 eV to 3.31–3.39 eV due to this dehydration mechanism. This abnormally large activation enthalpy is difficult to explain either by the proton conduction mechanism or the small polaron conduction mechanism. In the latter study, Hu et al. (2018) found a remarkable increase in the electrical conductivity of a single amphibole crystal at 843 K and 0.5–2 GPa (Figure 4), which was explained by the dehydrogenation of amphibole associated with the oxidation of iron from ferrous to ferric iron. However, the activation enthalpy decreased slightly after dehydrogenation of amphibole, which is completely different from what was reported by Wang et al. (2012). In contrast, Zhou et al. (2011) found that the electrical conductivity of natural amphibole-bearing rocks (amphibole content, 58 vol%) did not change rapidly at temperatures below 973 K. The activation enthalpy lies between 0.71 and 0.75 eV.

The findings in the present study are consistent with those of Zhou et al. (2011), in terms of before the dehydration melting of amphibole. Like Zhou et al., we did not observe a significant change in slope at low temperatures. The electrical conductivity of the sample containing amphibole higher than 60 wt% was consistent with that reported by Wang et al. (2012) and higher

than that reported by Hu et al. (2012), at temperatures less than 750 K, respectively. At temperatures higher than 900 K, the electrical conductivity of the sample containing amphibole higher than 60 wt% was comparable to that reported by Hu et al. (2018) and lower than that reported by Wang et al. (2012). The activation enthalpy was 0.59 and 1.05 eV, which is similar to that reported by Hu et al. (2018) and Wang et al. (2012), before dehydration or dehydrogenation of the amphibole. The inconsistencies in conductivity among different studies may result for several reasons. Water fugacity may be a key reason, except for pressure, conductivity anisotropy, and chemical composition of the starting material. A cell-assembly structure for conductivity measurement is usually invalid when closed conditions are required. As a result, the sample is always measured under low water fugacity. Such a chemical condition will reduce the stability of hydrous minerals. For example, Perrillat et al. (2005) reported that the temperature stability of antigorite under low water fugacity was reduced by 50–100 K, and its dehydration kinetics were much faster compared with those under water-saturated conditions. Recently, Guo et al. (2022) reported the partial dehydration of brucite single crystal, with a low water fugacity, at temperatures 300 K lower than those determined by phase equilibrium experiments. The BN capsule and MgO capsule used in this study and in the study by Zhou et al. (2011), respectively, may provide better closed conditions, in contrast with the $Al_2O_3$ capsule used by Hu et al. (2018) and Wang et al. (2012), which will cause a high waterer fugacity during high-temperature annealing of the sample. We propose that the abrupt changes in conductivity, as reported by Hu et al. (2018) and Wang et al. (2012), at relatively low temperatures, are due to the partial dehydration of amphibole under low water fugacity conditions. This partial dehydration is slow and does not destroy the crystal structure of the amphibole over a short experimental time scale.

289 **4.2 Conduction Mechanism**

290 The conduction mechanism for amphibole-bearing rocks varies with temperature. Before the
291 dehydration of the amphibole at 1100 K and 1.5 GPa, the electrical conductivity of amphibole-
292 bearing rocks was dominated by the electrical conductivity of the amphibole itself, which is
293 supported by the dependence of the bulk conductivity on the amphibole content in the sample
294 (Figure S4). The main conduction mechanism for amphibole is likely to be proton conduction, for
295 which the activation enthalpy is usually less than 1 eV. Proton conduction in hydrous minerals
296 with a layered structure usually occurs through a hydrogen-bond-type interaction between an $H'$
297 (extrinsic hydrogen vacancy) and any adjacent $OH^-$. Proton transfer can be expressed by:

298 $$H' + OH^- \rightarrow OH^- + H' \qquad (5)$$

299 where $H'$ corresponds to a defect proton (H vacancy forms in the hydroxide lattice, chemically $O^{2-}$
300 ), and $OH^-$ is the hydroxyl ion. A detailed discussion is reported elsewhere (Guo & Yoshino, 2013;
301 2014). A small polaron conduction mechanism may exist, but it is unlikely to be the dominant
302 conduction mechanism at the low temperatures of our experiment; this is supported by the small
303 activation enthalpy.

304 When the dehydration melting of amphibole begins, ionic conduction in the hydrous melt
305 becomes prevalent in the sample. Despite the melt's being rich in water, protons may not figure
306 significantly as electric charge carriers. Hydrogen mainly exists in the form of $H_2O$ molecules in
307 melts, or $H_2$ under extremely reducing conditions (Behrens et al., 2004). Both of these forms are
308 neutral species. The contribution of water in the melt to the bulk conductivity probably mainly
309 arises from the increased mobility of alkali ions in the hydrous melt (Gaillard, 2004). Previous
310 studies show that the migration of light alkali ions (e.g., $Na^+$ and $Li^+$) in silicate melts dominates
311 ionic conduction (Gaillard & Iacono-Marziano, 2005; Ni et al., 2011). The activation enthalpies

(0.59–1.05 eV) of the samples containing hydrous melts in this study are similar to those of pure hydrous melts containing more than 6.3 wt% $H_2O$ (Ni et al., 2011). In our study, therefore, we conclude that $Na^+$ transport dominates ionic conduction after dehydration melting of the amphibole occurs.

### 4.3 Geological Implication

Dehydration melting of amphibolite rocks can enhance the bulk conductivity to 1 S/m (Figure 5), which is the highest value observed in the crust of the Tibetan Plateau. Whether the model of the dehydration melting of amphibolite is responsible for the origin of LV-HCZs in the crust of the Tibetan Plateau or not requires the fulfillment of the following conditions: The first is that amphibolite dominates the rock type in the region where LV-HCZs exist. The second is that the temperature is high enough to initiate the dehydration melting of the amphibolites.

Amphibolite is one possible candidate for the genesis of adakite-like rocks, which are widespread in the postcollisional orogenic setting of the Lhasa block of the Tibetan Plateau (Lustrino et al., 2011; Wang et al., 2005; Wang et al., 2018), and which correspond to the phase equilibrium experiments (Qian & Hermann, 2013; Wang et al., 2019; Ye et al., 2021). The proof of xenoliths in Tibetan shoshonitic magmas (Hou et al., 2017) also supports the hypothesis that amphibolite is the main rock type in the lower crust of the Tibetan Plateau. Furthermore, deformed garnet amphibolite could be responsible for the strong seismic anisotropy that occurs in the mid-lower crust of the Tibetan Plateau (Tatham et al., 2008; Ji et al., 2015). The driving force for the deformation of amphibolite is likely to be the corner flow in the overlying mantle wedge induced by the subduction of the Indian lithospheric slab (Wu et al., 2019). Hence, amphibolite is a rock type that competes strongly with the generally accepted granulite in the mid-lower crust of the Tibetan Plateau.

335 The temperature beneath the Tibetan Plateau is not well known. However, the surface heat
336 flow is extremely high (Francheteau et al., 1984; Hu et al., 2000), and hot springs are
337 comprehensively found in South Tibet, indicating that the temperature of the Tibetan crust may be
338 high. In the northern Lhasa terrane, the estimated temperature is as high as 1073 K at a middle-
339 crust depth due to the seismic detection of the α-β quartz transition (Mechie et al., 2004). In a
340 recent study, Fu et al. (2019) calculated the temperature at 1.5 GPa to be higher than 1100 K (up
341 to 1350 K) based on the data of thermal conductivity measurements, assuming the heat flow and
342 the radiative heat production to be 80 $mW/m^2$ and 1.21 $\mu W/m^3$, respectively. Phase equilibrium
343 experiments have revealed that the dehydration melting of amphibolites starts at nearly 1123 K at
344 1.5 GPa (Wang et al., 2019). Consequently, dehydration melting of amphibolite is likely to occur
345 in the geotherm of the Tibetan lower crust.

346 The temperature of dehydration melting inferred from the conductivity measurements of
347 amphibole-bearing samples at 1.5 GPa in this study was about 1100 K (Figure 5). The bulk
348 conductivity of garnet amphibolite containing 60 wt% amphibole was as high as 0.1 S/m at 1200
349 K. Given that conductivity is measured in an open system, some water may have escaped during
350 measurement. The bulk conductivity of 0.1 S/m should be underestimated due to the enhancement
351 of water on the melt conductivity. The high-conductivity anomalies of 0.1–0.3 S/m present at a
352 depth of 50 km beneath Qiangtang Terrane (Wei et al., 2001; Le Pape et al., 2012) can be explained
353 by the dehydration melting of garnet amphibolite with an amphibole content higher than 60 wt%.
354 The highest conductivity anomaly of 1 S/m beneath eastern Tibet and in the Yarlung Tsangpo
355 Suture Zone in southern Tibet (Wei et al., 2001) is difficult to be explained by the dehydration
356 melting of amphibolite, which requires an amphibole content as high as 100 wt%. Dehydration
357 melting of felsic gneiss with a low concentration of amphibole is difficult to explain the high

conductivity of 0.1 S/m even at 1300 K. In contrast, dehydration melting of the basic lower crustal rock, such as garnet amphibolite, is more likely to be responsible for the high-conductivity anomalies. Partial dehydration of amphibole, as found by Wang et al. (2012) and Hu et al. (2018), seems to contribute to an electrical conductivity of around 0.1 S/m or more, even at low temperatures. However, the partial dehydration process is not the final state at equilibrium due to the high temperature characteristics in the lower crust of the Tibetan Plateau.

To quantitatively determine the melt fraction needed to explain the 0.1–1 S/m high-conductivity anomalies, we use a Maxwell-Wagner (MW) model to fit the experimental data of Amp100, Grt-Amp80, and Grt-Amp60 under isothermal conditions (1300 K) and to calculate the conductivity of the hydrous melt. The Maxwell-Wagner model is suitable for the case that a grain boundary shell of phase 1 surrounding a spherical grain of phase 2 (Figure 6). It gives the following expression for complex conductivity:

$$\sigma_{bulk} = \sigma_m \frac{2\sigma_m+\sigma_s-2(1-x_m)(\sigma_m-\sigma_s)}{2\sigma_m+\sigma_s+(1-x_m)(\sigma_m-\sigma_s)} \qquad (6)$$

where $\sigma_{bulk}$ is the bulk conductivity, $\sigma_m$ is the conductivity of melt, $\sigma_s$ is the conductivity of solid phase, and $x_m$ is the melt fraction. We counted the melt fraction in the rim part, which included the pure melt (melt$^a$) in the rim and the melt (melt$^b$) coexisting with quenched Opx. The composition of melt$^b$ should be similar to that of melt$^a$ because the quenched Opx should be dissolved in melt$^b$ before being quenched. Figure 7 shows the measured bulk conductivity versus the measured melt fraction together with the fitting result using the MW model. MW fitting yields values of 3.86 S/m and 7.13E-3 S/m for the melt and the solid phase, respectively, at 1300 K and 1.5 GPa. As the natural melt distribution in the deep Earth can be better simulated by cube model, which assumes that cubic grains are surrounded by a melt layer with a uniform thickness dependent on the melt fraction and the conductivities of the solid phases are negligibly small, we again

calculated the bulk conductivities through a cube model simulation. The bulk conductivity ($\sigma_{bulk}$) is given by:

$$\sigma_{bulk} = [1 - (1 - \Phi)^{\frac{2}{3}}]\sigma_m \qquad (7)$$

where $\Phi$ is the melt fraction in volume. The bulk conductivities obtained from these two models are very similar when the melt fraction is higher than 1%. To account for the high conductivity anomalies of 0.1 and 1 S/m at 1300 K and 1.5 GPa, melt fractions of 3.8% and 36% are necessary, respectively. It should be noted that some water may escapes from the system and the dissolved boron component will restrain the bulk conductivity of the sample (viscosity increases due to the dissolved boron in the melt). Therefore, the melt fractions of the partial molten region in the mid-lower crust of the Tibetan Plateau should be lower than the current calibrated ones.

One challenge of using the dehydration melting model of amphibolite is how the buoyant hydrous melt to retain within the mid-lower crust. The dihedral angle of a possible solid-solid-fluid system plays a key role in this challenge. If the dihedral angle was more than 60°, the fluid would not form an interconnected network and might be trapped as interstitial fluid in the solid phase. Experimental data shows that the dihedral angle is larger than 60° for upper-mantle peridotite (Mibe et al., 1999), pyroxene-rich rocks (Watson & Lupulescu, 1993), and eclogite (Mibe et al., 2003) under the conditions comparable to ours. This means that the fluid phase can be well retained at depth of interest. It may be argued that low connectivity will inevitably lead to a low conductivity. However, in case of the mid-lower crust of Tibetan Plateau, the large-scale flow of lower crust (Bai et al., 2010), resulted from the ongoing collision of the Indian and Asian continents, will generate the channel-like melt distribution (Holtzman et al., 2003), which can cause the high conductivity parallel to the extension direction and the conductivity anisotropy (Zhang et al., 2014).

As different types of igneous rocks are all discovered in the Tibetan Plateau, we compared the conductivities of hydrous melts in this study with those of hydrous rhyolitic, andesitic and basaltic melts in previous studies. Figure 8 shows the electrical conductivity of different types of melts versus NBO/T values (the number of nonbridging oxygen ions per tetrahedrally coordinated cation, indicating the degree of depolymerization). The electrical conductivity of the andesitic melt with higher NBO/T (Guo et al., 2017) is higher than that of rhyolitic melt with lower NBO/T (Guo et al., 2016), indicating higher degree of depolymerization leads to a lower viscosity, and therefore greater ion mobility and high conductivity. The conductivity versus the NBO/T in this study seems to follow this trend despite the water content, not well constrained, is a little higher. In contrast, the conductivity of basaltic melt with highest NBO/T (Ni et al., 2011) is lowest, which is against the depolymerization consideration. The reason may be resulted from the pressure difference, the compositional difference in melts, and/or inapposite extrapolation of the data from high temperature to low temperature. If we believe the relationship between conductivity and NBO/T, the basaltic melt, the products of high degree partial melting of the crustal rock, is more conductive and therefore more easily to contribute to the high conductivity anomalies within the crust of the Tibetan Plateau.

## 5 Conclusions

In this study, the electrical conductivities of amphibole-bearing samples were measured by means of complex impedance spectroscopy at 1.5 GPa and 600–1300 K. The dehydration melting of (garnet-) amphibolite with an amphibole content as high as 60 wt% at around 1100 K, which is defined by electrical conductivity measurements, enhances the bulk conductivity to a value comparable to the high-conductivity anomalies of 0.1 S/m observed in the mid-lower crust of the Tibetan Plateau. Consequently, a model that uses the dehydration melting of amphibolite is as

successful as models that use fluid, graphite film, and sulfide in explaining these high-conductivity anomalies. In particular, in regions where the surface heat flow is high, the dehydration melting model is likely to be successful and can explain both the high conductivity and the low velocity anomalies in the mid-lower crust of the Tibetan Plateau. The estimated melt volume fractions of the partial molten region are 3.8–36 vol%, accounting for the high-conductivity anomalies of 0.1–1 S/m arising from a cube-model simulation.

## Acknowledgments

We thank Jihao Zhu for the technical support during EPMA analysis. This study was supported by the National Key Research and Development Project of China (project 2016YFC0600309), the CAS "Light of West China" program (Y9CR026 to X. G.), and the National Natural Science Foundation of China (No. 442072051). Per AGU's Data Policy, the supporting date has been deposited in a general repository, Zenodo (doi: 10.5281/zenodo.6219836).

## References

Bai, D., Unsworth, M.J., Meju, M.A., Ma, X., Teng, J., Kong, X., Sun, Y., Sun, J., Wang, L., Jiang, C., Zhao, C., Xiao, P., & Liu, M. (2010). Crustal deformation of the eastern Tibetan plateau revealed by magnetotelluric imaging. *Nature Geoscience*, *3*, 358–362. https://doi.org/10.1038/NGEO830

Behrens, H., Zhang, Y., & Xu, Z. (2004). $H_2O$ diffusion in dacitic and andesitic melts. *Geochimica et Cosmochimica Acta*, *68*, 5139–5150. https://doi.org/10.1016/j.gca.2004.07.008

Chen, S., Guo, X., Yoshino, T., Jin, Z. & Li, P. (2018). Dehydration of phengite inferred by electrical conductivity measurements: Implication for the high conductivity anomalies relevant to the subduction zones. *Geology*, *46*, 11–14. https://doi.org/10.1130/G39716.1

449 Francheteau, J., Jaupart, C., Shen, X.J., Kang, W.H., Lee, D.L., Bai, J.C., Wei, H.P., & Deng, H.Y.
450 (1984). High heat flow in southern Tibet. *Nature, 307,* 32–36.
451 https://doi.org/10.1038/307032a0
452 Fu, H., Zhang, B., Ge, J., Xiong, Z., Zhai, S., & Li, H. (2019). Thermal diffusivity and thermal
453 conductivity of granitoids at 2283–988 K and 0.3–1.5 GPa. *American Mineralogist, 104,*
454 1533–1545. https://doi.org/10.2138/am-2019-7099
455 Fuji-ta, K., Katsura, T., & Tainosho, Y. (2004). Electrical conductivity measurement of granulite
456 under mid-to-lower crustal pressure-temperature conditions. *Geophysical Journal*
457 *International, 157*(1), 79–86. https://doi.org/10.1111/j.1365-246X.2004.02165.x
458 Gaillard, F. (2004). Laboratory measurements of electrical conductivity of hydrous and dry silicic
459 melts under pressure. *Earth and Planetary Science Letters, 218,* 215–228.
460 https://doi.org/10.1016/S0012-821X(03)00639-3
461 Gaillard, F., & Iacono-Marziano, G. (2005). Electrical conductivity of magma in the course of
462 crystallization controlled by their residual liquid composition. *Journal of Geophysical*
463 *Research: Solid Earth, 110,* B06204. https://doi.org/10.1029/2004JB003282.
464 Guo, X., & Yoshino, T. (2013). Electrical conductivity of dense hydrous magnesium silicates with
465 implication for conductivity in the stagnant slab. *Earth and Planetary Science Letters, 369–*
466 *370,* 239–247. https://doi.org/10.1016/j.epsl.2013.03.026
467 Guo, X., & Yoshino, T. (2014). Pressure-induced enhancement of proton conduction in brucite.
468 *Geophysical Research Letters, 441,* 813–819. https://doi.org/10.1002/2013GL058627
469 Guo, X., Li, B., Ni, H., & Mao, Z. (2017). Electrical conductivity of hydrous andesitic melts
470 pertinent to subduction zones. *Journal of Geophysical Research: Solid Earth, 122,* 1777–
471 1788. https://doi.org/10.1002/2016JB013524

Guo, X., Yoshino, T., & Shimojuku, A. (2015). Electrical conductivity of albite–(quartz) –water and albite–water–NaCl systems and its implication to the high conductivity anomalies in the continental crust. *Earth and Planetary Science Letters*, *412*, 1–9. https://doi.org/10.1016/j.epsl.2014.12.021

Guo, X., Yoshino, T., Chen, S., Wu, X., & Zhang, J. (2022). Partial dehydration of brucite and its implications for water distribution in the subducting oceanic slab. *Geoscience Frontiers, 13 (2)*, 101342. https://doi.org/10.1016/j.gsf.2021.101342

Guo, X., Zhang, L., Behrens, H., & Ni, H. (2016). Probing the status of felsic magma reservoirs: Constraints from the *P*–*T*–$H_2O$ dependences of electrical conductivity of rhyolitic melt. *Earth and Planetary Science Letters*, *433*, 54–62. https://doi.org/10.1016/j.epsl.2015.10.036

Hacker, B.R., Ritzwoller, M.H., & Xie, J. (2014). Partially melted, mica-bearing crust in Central Tibet. *Tectonics*, *33*, 1408–1424. https://doi.org/10.1002/2014TC003545

Holtzman, B.K., Kohlstedt, D.L., Zimmerman, M.E., Heidelbach, F., Hiraga, T., & Hustoft, J. (2003). Melt segregation and strain partitioning: implications for seismic anisotropy and mantle flow. *Science*, *301*, 1227–1230. https://doi.org/10.1126/science.1087132.

Hou, Z., Zhou, Y., Wang, R., Zheng, Y., He, W., Zhao, M., Evans, N.J., & Weinberg, R.F. (2017). Recycling of metal-fertilized lower continental crust: Origin of non-arc Au-rich porphyry deposits at cratonic edges. *Geology*, *45*, 563–566. https://doi.org/10.1130/G38619.1

Hu, H., Dai, L., Li, H., Sun, W., & Li, B. (2018). Effect of dehydrogenation of the electrical conductivity of Fe-bearing amphibole: Implications for high conductivity anomalies in subduction zones and continental crust. *Earth and Planetary Science Letters*, *498*, 27–37. https://doi.org/10.1016/j.epsl.2018.06.003

494 Hu, S., He, L., & Wang, J. (2000). Heat flow in the continental area of China: A new data set.
495 *Earth and Planetary Science Letters, 179*, 407–419. https://doi.org/10.1016/S0012-
496 821X(00)00126-6
497 Ji, S.C., Shao, T., Michibayashi, K., Oya, S., Satsukawa, T., Wang, Q., Zhao, W., & Salisbury,
498 M.H. (2015). Magnitude and symmetry of seismic anisotropy in mica- and amphibole-bearing
499 metamorphic rocks and implications for tectonic interpretation of seismic data from the
500 southeast Tibetan Plateau. *Journal of Geophysical Research*, *120*, 6404–6430.
501 https://doi.org/10.1002/2015JB012209
502 Kang, D., Zhang, Z., Palin, R.M., Tian, Z., & Dong, X. (2019). Prolonged partial melting of garnet
503 amphibolite from the eastern Himalayan Syntaxis: Implications for the tectonic evolution of
504 large hot orogens. *Journal of Geophysical Research: Solid Earth*, *125*, 1–22.
505 https://doi.org/10.1029/2019JB019119
506 Kariya, K.A., & Shankland, T.J. (1983). Electrical conductivity of dry lower crustal rocks.
507 *Geophysics*, *48*, 52–61. https://doi.org/10.1190/1.1441407
508 Le Pape, F., Jones, A.G., Vozar, J., & Wei, W. (2012). Penetration of crustal melt beyond the
509 Kunlun Fault into northern Tibet. *Nature Geoscience*, 5, 330–335.
510 https://doi.org/10.1038/NGEO1449
511 Li, P., Guo, X., Chen, S., Wang, C., Yang, J., & Zhou, X. (2018). Electrical conductivity of the
512 plagioclase-NaCl-water system and its implication for the high conductivity anomalies in the
513 mid-lower crust of Tibet Plateau. *Contributions to Mineralogy and Petrology*, *173*, 16.
514 https//doi.org/10.1007/s00410-018-1442-9

Lustrino, M., Duggen, S., & Rosenberg, C.L. (2011). The Central-Western Mediterranean: Anomalous igneous activity in an anomalous collisional tectonic setting. *Earth-Science Reviews, 104,* 1–40. https//doi.org/10.1016/j.earscirev.2010.08.002

Makovsky, Y., & Klemperer, S.L. (1999). Measuring the seismic properties of Tibetan bright spots: Evidence for free aqueous fluids in the Tibetan middle crust. *Journal of Geophysical Research: Solid Earth, 104,* 10795–10825. https://doi.org/10.1029/1998JB900074

Manthilake, G., Mookherjee, M., Bolfan-Casanova, N., & Andrault, D. (2015). Electrical conductivity of lawsonite and dehydrating fluids at high pressures and temperatures. *Geophysical Research Letters, 42,* 7398–7405. https://doi.org/10.1002/2015GL064804.

Mechie, J., Sobolev, S.V., Ratschbacher, L., Babeyko, A.Y., Bock, G., Jones, A.G., Nelson, K.D., Solon, K.D., Brown, L.D., & Zhao, W. (2004). Precise temperature estimation in the Tibetan crust from seismic detection of the α-β quartz transition. *Geology, 32,* 601–604. http://doi.org/10.1130/G20367.1.

Mibe, K., Fuji, T., & Yasuda, A. (1999). Control of the location of the volcanic front in island arcs by aqueous fluid connectivity in the mantle wedge. *Nature, 401,* 259–262.

Mibe, K., Yoshino, T., Ono, S., Yasuda, A., & Fuji, T. (2003). Connectivity of aqueous fluid in eclogite and its implications for fluid migration in the Earth's interior. *Journal of Geophysical Research: Solid Earth, 108(B6).* https://doi.org/10.1029/2002JB001960

Nelson, K.D., Zhao, W., Brown, L.D., Kuo, J., Che, J., Liu, X., Klemperer, S.L., Makovsky, Y., Meissner, R., Mechie, J., Kind, R., Wenzel, F., Ni, J., Nabelek, J., Chen, L., Tan, H., Wei, W., Jones, A.G., Booker, J., Unsworth, M., Kidd, W.S.F., Hauck, M., Alsdorf, D., Ross, A., Gogan, M., Wu, C., Sandvol, E., & Edwards, M. (1996). Partially molten middle crust

beneath Southern Tibet: Synthesis of project INDEPTH results. *Science*, *274*, 1684–1688. http://doi.org/10.1126/science.274.5293.1684

Ni, H., Keppler, H., & Behrens, H. (2011). Electrical conductivity of hydrous basaltic melts: Implications for partial melting in the upper mantle. *Contributions to Mineralogy and Petrology*, *162*, 637–650. http://doi.org/10.1007/s00410-011-0617-4

Olhoeft, G.R. (1981). Electrical properties of granite with implications for the lower crust. *Journal of Geophysical Research*, *86*, 931–936. http://doi.org/10.1029/JB086iB02p00931

Ozacar, A.A., & Zandt, G. (2004). Crustal seismic anisotropy in central Tibet: Implications for deformation style and flow in the crust. *Geophysical Research Letters*, *31*, L23601. http://doi.org/10.1029/2004GL021096

Perrillat, J., Daniel, I., Koga, K.T., Reynard, B., Cardon, H., & Crichton, W.A. (2005). Kinetics of antigorite dehydration: A real-time X-ray diffraction study. *Earth and Planetary Science Letters*, *236*, 899–913. http://doi.org/10.1016/j.epsl.2005.06.006

Qian, Q., & Hermann, J. (2013). Partial melting of lower crust at 10-15 kbar: Constraints on adakite and TTG formation. *Contributions to Mineralogy and Petrology*, *165*, 1195–1224. http://doi.org/10.1007/s00410-013-0854-9

Roberts, J.J., & Tyburczy, J.A. (1991). Frequency dependent electrical properties of polycrystalline olivine compacts. *Journal of Geophysical Research*, *96*, 16205–16222. http://doi.org/10.1029/91JB01574

Roger, F., Tapponnier, P., Arnaud, N., Schärer, U., Brunel, M., Xu, Z., & Yang, J. (2000). An Eocene magmatic belt across central Tibet: Mantle subduction triggered by the Indian collision? *Terra Nova*, *12*, 102–108. http://doi.org/10.1046/j.1365-3121.2000.123282.x

559 Shapiro, N.M., Ritzwoller, M.H., Molnar, P., & Lvein, V. (2004). Thinning and flow of Tibetan
560 crust constrained by seismic anisotropy. *Science*, *305*, 233–236.
561 http://doi.org/10.1126/science.1098276
562 Shimojuku, A., Yoshino, T., Yamazaki, D., & Okudaira, T. (2012). Electrical conductivity of fluid-
563 bearing quartzite under lower crustal conditions. *Physics of the Earth and Planetary Interiors*,
564 *198–199*, 1–8. http://doi.org/10.1016/j.pepi.2012.03.007
565 Takahashi, E., & Scarfe, C.M. (1985). Melting of peridotite to 14 GPa and the genesis of komatiite.
566 *Nature*, *315*, 566-568. http://doi.org/10.1038/315566a0
567 Tapponnier, P., Xu, Z., Roger, F., Meyer, B., Arnaud, N., Wittlinger, G., & Yang, J. (2001).
568 Oblique stepwise rise and growth of the Tibet plateau. *Science*, *294*, 1671–1677.
569 http://doi.org/10.1126/science.105978
570 Unsworth, M.J., Jones, A.G., Wei, W., Marquis, G., Gokarn, S.G., Spratt, J.E., Bedrosian, P.,
571 Booker, J., Chen, L., Clarke, G., Li, S., Lin, C., Deng, M., Jin, S., Solon, K., Tan, H., Ledo,
572 J., & Roberts, B. (2005). Crustal rheology of the Himalaya and Southern Tibet inferred from
573 magnetotelluric data. *Nature*, *438*, 78–81. http://doi.org/10.1038/nature04154
574 Waff, H.S. (1974). Theoretical considerations of electrical conductivity in a partially molten
575 mantle and implications for geothermometry. *Journal of Geophysical Research*, *79*, 4003–
576 4010. http://doi.org/10.1029/JB079i026p04003
577 Wang, D., Guo, Y., Yu, Y., & Karato, S. (2012). Electrical conductivity of amphibole-bearing
578 rocks: Influence of dehydration. *Contributions to Mineralogy and Petrology*, *164*, 17–25.
579 http://doi.org/10.1007/s00410-012-0722-z
580 Wang, Q., Hawkesworth, C.J., Wyman, D., Wyman, D., Chung, S., Wu, F., Li, X., Li, Z., Gou, G.,
581 Zhang, X., Tang, G., Dan, W., Ma, L., & Dong, Y. (2016). Pliocene-Quaternary crustal

582 melting in central and northern Tibet and insights into crustal flow. *Nature Communications*,
583 *7*, 11888. https://doi.org/10.1038/ncomms11888.
584 Wang, Q., McDermott, F., Xu, J.F., Bellon, H., & Zhu, Y.T. (2005). Cenozoic K-rich adakitic
585 volcanic rocks in the Hohxil area, northern Tibet: Lower crustal melting in an intracontinental
586 setting. *Geology*, *33*, 465. https://doi.org/10.1130/g21522.1
587 Wang, R., Weinberg, R.F., Collins, W.J., Richards, J.P., & Zhu, D.C. (2018). Origin of
588 postcollisional magmas and formation of porphyry Cu deposits in southern Tibet. *Earth-*
589 *Science Reviews*, *181*, 122–143. https://doi.org/10.1016/j.earscirev.2018.02.019
590 Wang, X., Zhang, J., Rushmer, T., Adam, J., Turner, S., & Xu, W. (2019). Adakite-like potassic
591 magmatism and crust-mantle interaction in a postcollisional setting: An experimental study
592 of melting beneath the Tibetan Plateau. *Journal of Geophysical Research: Solid Earth*, *124*.
593 https://doi.org/10.1029/2019JB018392
594 Watson, E.B., & Lupulescu, A.. (1993). Aqueous fluid connectivity and chemical transport in
595 clinopyroxene-rich rocks. *Earth and Planetary Science Letters*, *117*, 279–294
596 Wei, W., Unsworth, M.J., Jones, A.G., Booker, J., Tan, H., Nelson, D., Chen, L., Li, S., Solon, K.,
597 Bedrosian, P., Jin, S., Deng, M., Ledo, J.J., Kay, D., & Roberts, B. (2001) Detection of
598 widespread fluids in the Tibetan crust by magnetotelluric studies. *Science*, *292*, 716–718.
599 https://doi.org/10.1126/science.1010580
600 Yang, X., Keppler, H., Mccammon, C., & Ni, H. (2012). Electrical conductivity of orthopyroxene
601 and plagioclase in the lower crust. *Contributions to Mineralogy and Petrology*, *163*, 33–48.
602 https://doi.org/10.1007/s00410-011-0657-9
603 Ye, Z., Wan, F., Jiang, N., Xu, J., Wen, Y., Fan, D., & Zhou, W. (2021). Dehydration melting of
604 amphibolite at 1.5 GPa and 800–950 °C: Implications for the Mesozoic potassium-rich

adakite in the eastern North China Craton. *Geoscience Frontiers*, *12(2)*, 896–906. https://doi.org/10.1016/j.gsf.2020.03.008

Yoshino, T., & Noritake, F. (2011). Unstable graphite films on grain boundaries in crustal rocks. *Earth and Planetary Science Letters*, *306*, 186–192. https://doi.org/10.1016/j.epsl.2011.04.003

Yoshino, T., Laumonier, M., McIsaac, E., & Katsura, T. (2010). Electrical conductivity of basaltic and carbonatite melt-bearing peridotites at high pressures: Implications for melt distribution and melt fraction in the upper mantle. *Earth and Planetary Science Letters*, 295, 593–602

Zhang, B., Yoshino, T., Yamazaki, D., Manthilake, G., & Katsura, T. (2014). Electrical conductivity anisotropy in partially molten peridotite under shear deformation. *Earth and Planetary Science Letters*, *405*, 98–109. https://dx.doi.org/10.1016/j.epsl.2014.08.018

Zhang, Z., Dong, X., Xiang, H, Ding, H., He, Z., & Liou, J.G. (2015). Reworking of the Gangdese magmatic arc, southeastern Tibet: Post-collisional metamorphism and anatexis. *Journal of Metamorphic Geology*, *33*, 1–21. https://doi.org/10.1111/jmg.12107

Zhou, W., Fan, D., Liu, Y., & Xie, H. (2011). Measurements of wave velocity and electrical conductivity of an amphibolite from southwestern margin of the Tarim Basin at pressures to 1.0 GPa and temperatures to 700 °C: Comparison with field observations. *Geophysical Journal International*, *187*, 1393–1404. https://doi.org/10.1111/j.1365-246X.2011.05220.x

**Figure captions**

Fig. 1 Electrical conductivity of Amp25-Pl as a function of time. Temperatures at which the electrical conductivities are measured are shown in the figure. Above 1100 K, the electrical conductivity increases with time, indicating the partial dehydration initiates.

628

629 Fig. 2 Electrical conductivity of polycrystalline amphibole (Amp100) as a function of reciprocal
630 temperature. Electrical conductivities are measured during several heating–cooling cycles. After
631 the onset of dehydration melting, the activation enthalpy decreases from 0.85 eV in the high-
632 temperature region to 0.055 eV in the low-temperature region. The extremely low activation
633 enthalpy at 900–600 K is due to the exsolution of water from the melt.

634

635 Fig. 3 Representative textures of the recovered samples. The run products of the sample containing
636 25 vol% amphibole (Amp25-Pl) include Grt, Cpx, Pl, quench Opx, melt, and Il (a, b, and c). The
637 run products of the polycrystalline amphibole (Amp100) include Grt, Cpx, quench Opx, and melt
638 (d, e, and f). The melt can be divided into a, b, and c types due to the differences in distribution,
639 paragenesis, and chemical composition. For the garnet amphibolite (Grt-Amp60), the run products
640 are similar to those of Amp100, except that the melt fraction is lower (g, h, and i). Abbreviation:
641 Amp, amphibole; Grt, garnet; Pl, plagioclase; Cpx, clinopyroxene; Opx, orthopyroxene.

642

643 Fig. 4 Comparison between the electrical conductivities of amphibole-bearing rocks in this study
644 and those of other studies at temperatures below 1000 K. Symbols with colors represent the data
645 in this study. The black solid lines, dashed lines, dotted lines, and dashed-dotted lines represent
646 the data from the other studies. The numbers are the activation enthalpies. HDLSL18, Hu et al.,
647 2018. WGYK12, Wang et al., 2012.

648

649 Fig. 5 Comparison between the electrical conductivities of amphibole-bearing samples with
650 varying amphibole content in this study and the high-conductivity anomalies in the mid-lower

crust of the Tibetan Plateau. The symbols represent the data in this study. The different lines represent the data from previous studies. The yellow region represents the high-conductivity anomalies observed beneath the Tibetan Plateau. The grey region indicates the temperatures at which the dehydration melting of amphibole occurs. HDLSL18, Hu et al., 2018. WGYK12, Wang et al., 2012.

Fig. 6 The geometry of Maxwell-Wagner (MW) model. The MW model is suitable for the case that a grain boundary shell of phase 1 surrounding a spherical grain of phase 2.

Fig. 7 MW model fitting of the experimental results of (Grt-) amphibolite and cube model simulation at 1300 K and 1.5 GPa. The numbers indicate the melt fractions accounting for the high-conductivity anomalies (yellow region) in the mid-lower crust of the Tibetan Plateau.

Fig. 8 Relationship between the electrical conductivities of hydrous melts at 1300 K and 1.5 GPa (2 GPa for basalt) and the number of nonbridging oxygen ions per tetrahedrally coordinated cation (NBO/T). $\frac{\mathrm{NBO}}{\mathrm{T}} = \frac{\mathrm{O^{2-}} \times 2 - \mathrm{T} \times 4}{\mathrm{T}}$, where $O^{2-}$ represents the total number of $O^{2-}$ in mole, T is the total number of $Si^{4+}$ and $Al^{3+}$ in mole. The water content of melt[c], with a lowest boron contamination from the capsule, was used for comparison in this study. GZBN16, Guo et al., 2016; GLNM17, Guo et al., 2017; NKB11, Ni et al., 2011.

Table 1. Experimental conditions and results.

Table 2. Major element compositions (wt%) of residual major minerals.

Table 3. Chemical composition of the melts.

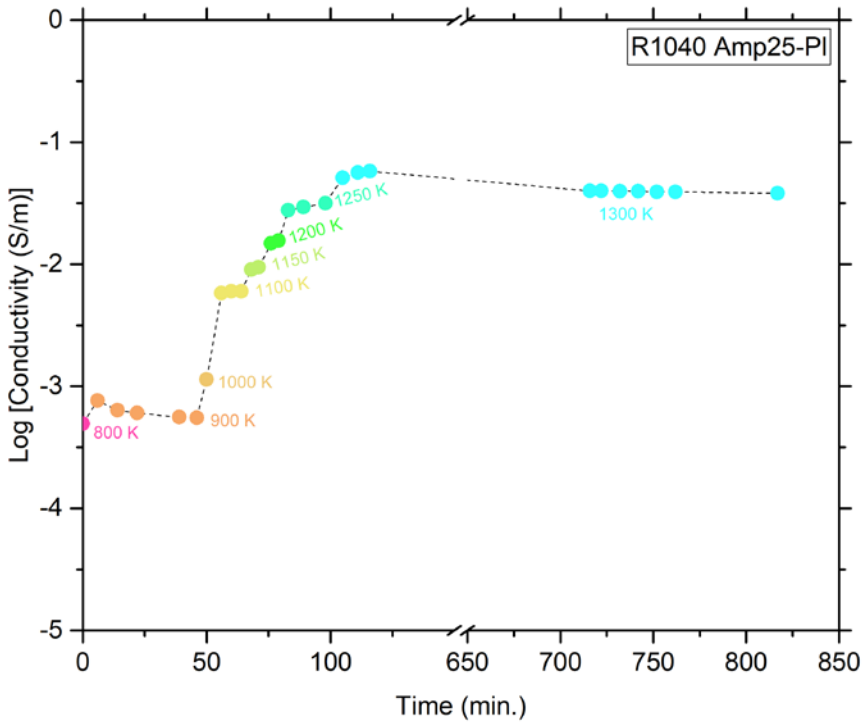
R1040 Amp25-Pl
Log [Conductivity (S/m)]
Time (min.)
0
-1
-2
-3
-4
-5
0
50
100
650
700
750
800
850
800 K
900 K
1000 K
1100 K
1150 K
1200 K
1250 K
1300 K

Figure 1

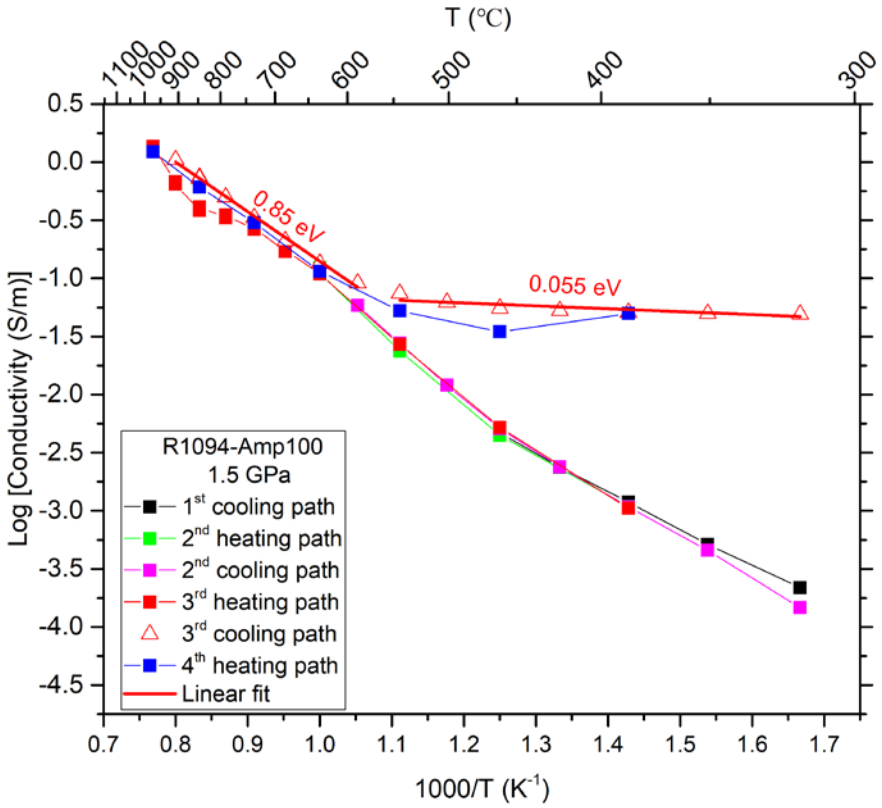
T (°C)
1100
1000
900
800
700
600
500
400
300
0.5
0.0
-0.5
-1.0
-1.5
-2.0
-2.5
-3.0
-3.5
-4.0
-4.5
Log [Conductivity (S/m)]
0.85 eV
0.055 eV
R1094-Amp100
1.5 GPa
1st cooling path
2nd heating path
2nd cooling path
3rd heating path
3rd cooling path
4th heating path
Linear fit
0.7
0.8
0.9
1.0
1.1
1.2
1.3
1.4
1.5
1.6
1.7
1000/T (K-1)

Figure 2

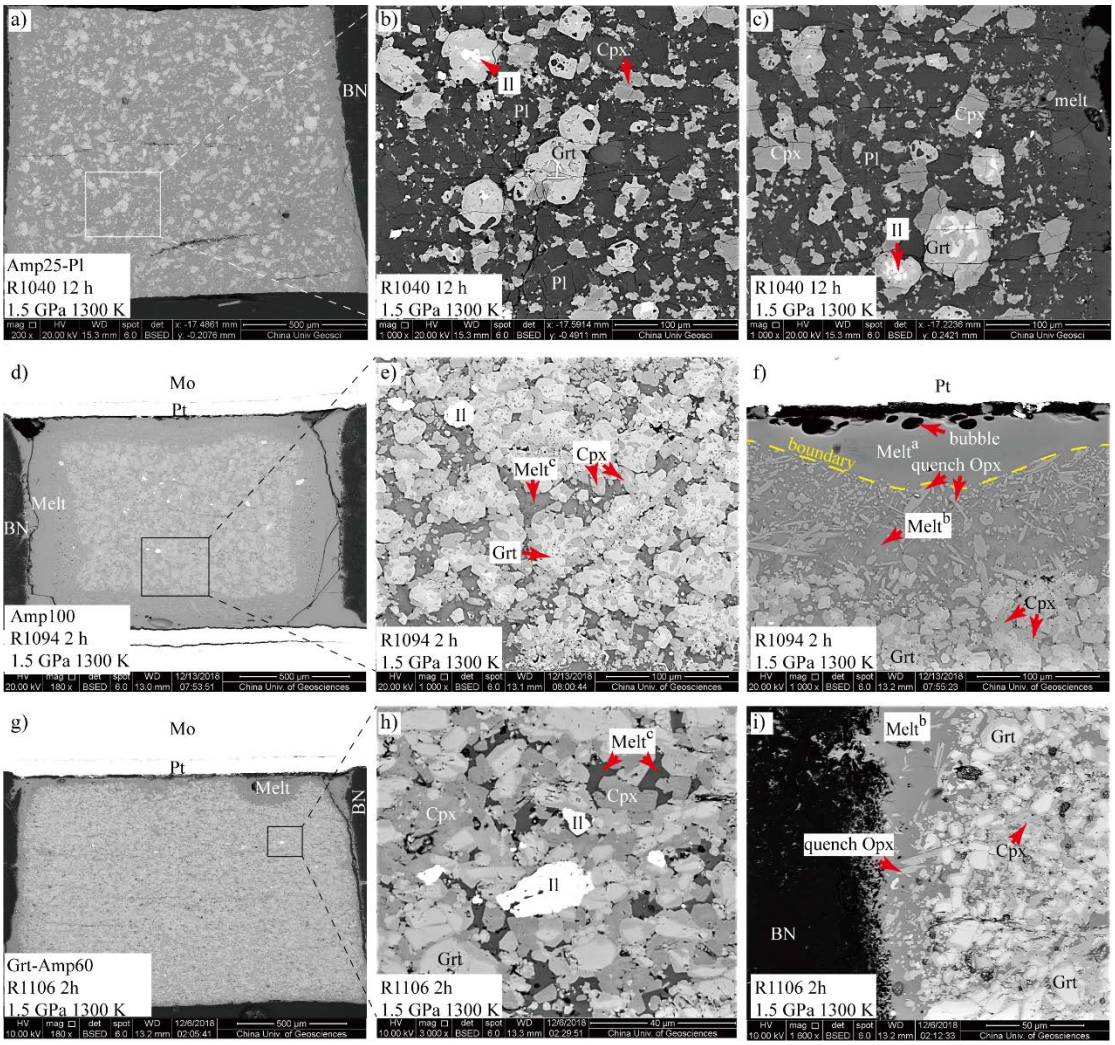
a)
BN
Amp25-Pl
R1040 12 h
1.5 GPa 1300 K
b)
Cpx
Il
Pl
Grt
R1040 12 h
1.5 GPa 1300 K
c)
melt
Cpx
Cpx
Pl
Il
Grt
R1040 12 h
1.5 GPa 1300 K
d)
Mo
Pt
Melt
BN
Amp100
R1094 2 h
1.5 GPa 1300 K
e)
Il
Melt^c
Cpx
Grt
R1094 2 h
1.5 GPa 1300 K
f)
Pt
boundary
Melt^a
bubble
quench Opx
Melt^b
Cpx
Grt
R1094 2 h
1.5 GPa 1300 K
g)
Mo
Pt
Melt
BN
Grt-Amp60
R1106 2h
1.5 GPa 1300 K
h)
Melt^c
Cpx
Cpx
Il
Il
Grt
R1106 2h
1.5 GPa 1300 K
i)
Melt^b
Grt
quench Opx
Cpx
BN
Grt
R1106 2h
1.5 GPa 1300 K

Figure 3

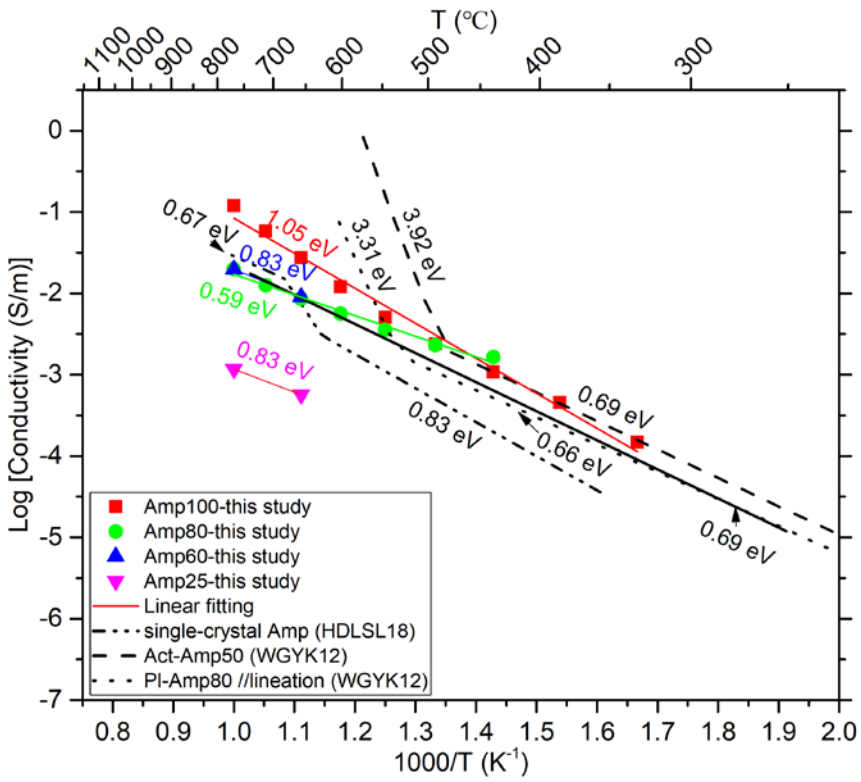
T (°C)
1100
1000
900
800
700
600
500
400
300
Log [Conductivity (S/m)]
0
-1
-2
-3
-4
-5
-6
-7
0.8
0.9
1.0
1.1
1.2
1.3
1.4
1.5
1.6
1.7
1.8
1.9
2.0
1000/T (K-1)
0.67 eV
1.05 eV
3.31 eV
3.92 eV
0.83 eV
0.59 eV
0.83 eV
0.69 eV
0.83 eV
0.66 eV
0.69 eV
Amp100-this study
Amp80-this study
Amp60-this study
Amp25-this study
Linear fitting
single-crystal Amp (HDLSL18)
Act-Amp50 (WGYK12)
Pl-Amp80 //lineation (WGYK12)

Figure 4

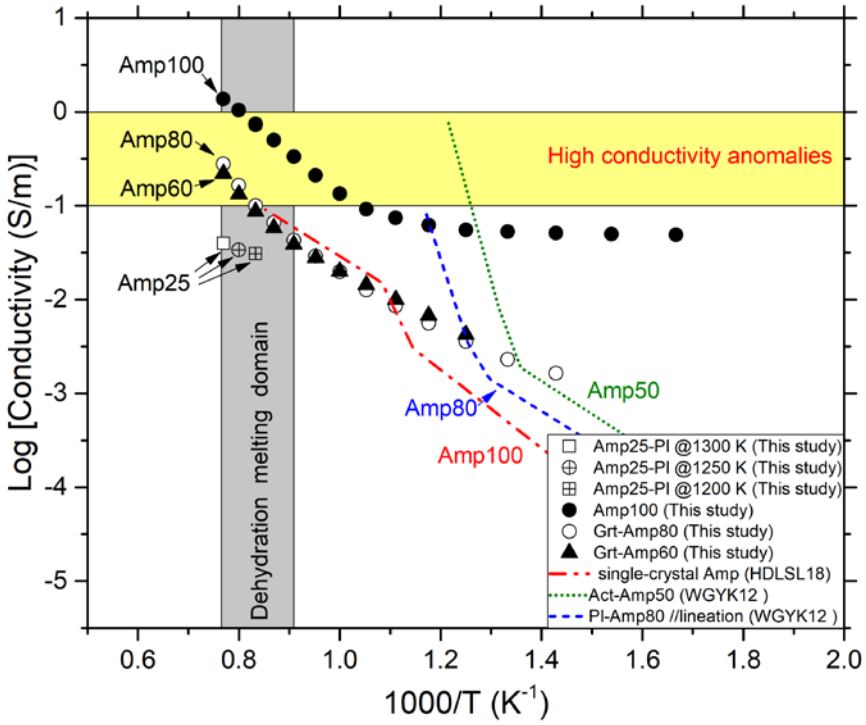
Amp100
Amp80
Amp60
Amp25
High conductivity anomalies
Dehydration melting domain
Amp50
Amp80
Amp100
Amp25-PI @1300 K (This study)
Amp25-PI @1250 K (This study)
Amp25-PI @1200 K (This study)
Amp100 (This study)
Grt-Amp80 (This study)
Grt-Amp60 (This study)
single-crystal Amp (HDLSL18)
Act-Amp50 (WGYK12 )
PI-Amp80 //lineation (WGYK12 )
Log [Conductivity (S/m)]
1000/T (K-1)
1
0
-1
-2
-3
-4
-5
0.6
0.8
1.0
1.2
1.4
1.6
1.8
2.0

Figure 5

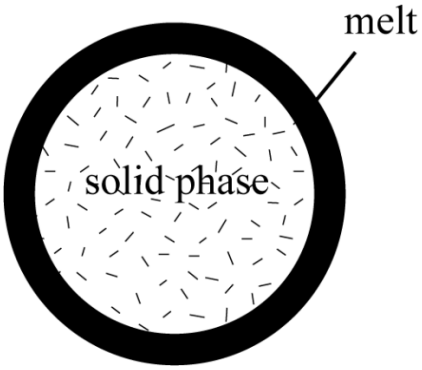


744

745 Figure 6

746

747

748

749

750

751

752

753

754

755

756

757

758

759

760

761

762

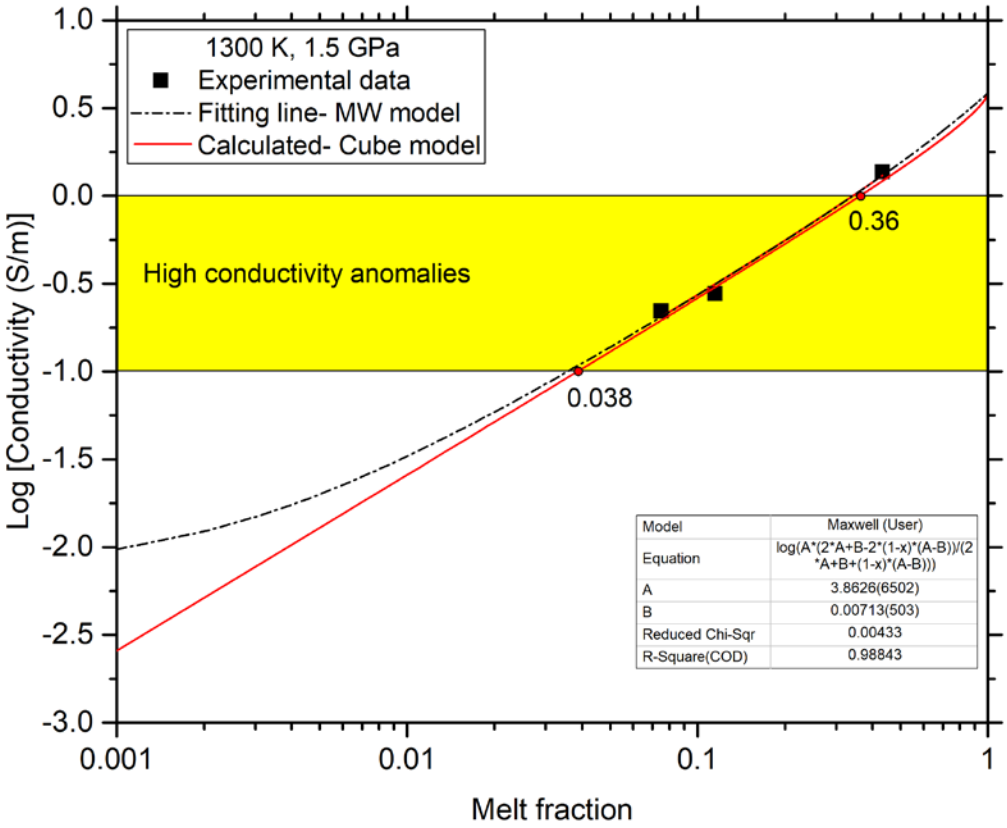
1300 K, 1.5 GPa
Experimental data
Fitting line- MW model
Calculated- Cube model
High conductivity anomalies
0.038
0.36
Model
Maxwell (User)
Equation
log(A*(2*A+B-2*(1-x)*(A-B))/(2*A+B+(1-x)*(A-B)))
A
3.8626(6502)
B
0.00713(503)
Reduced Chi-Sqr
0.00433
R-Square(COD)
0.98843
Log [Conductivity (S/m)]
Melt fraction
1.0
0.5
0.0
-0.5
-1.0
-1.5
-2.0
-2.5
-3.0
0.001
0.01
0.1
1

Figure 7

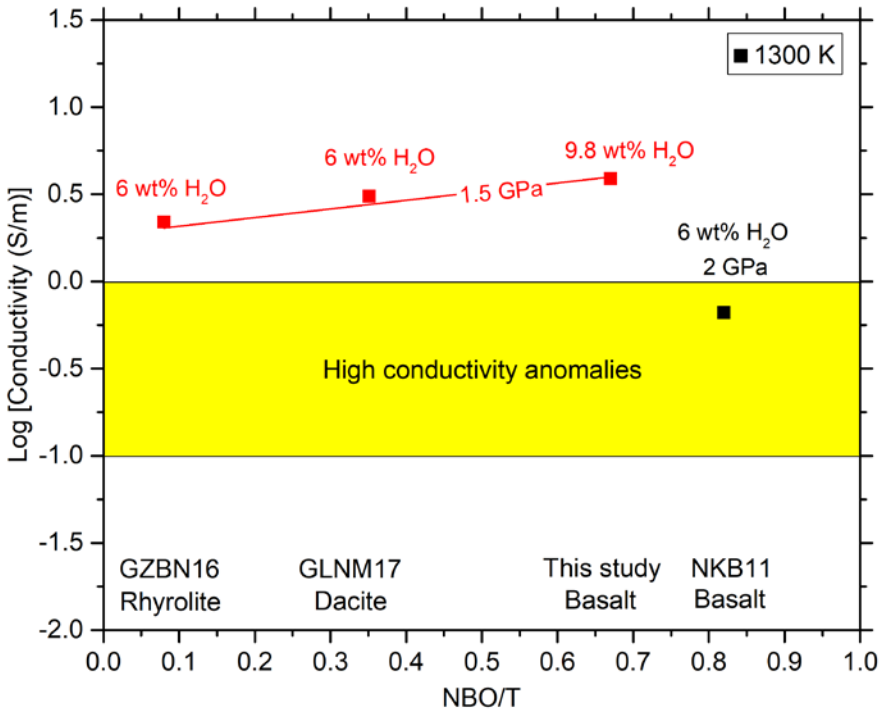
1300 K
6 wt% H2O
6 wt% H2O
9.8 wt% H2O
1.5 GPa
6 wt% H2O
2 GPa
High conductivity anomalies
GZBN16
Rhyrolite
GLNM17
Dacite
This study
Basalt
NKB11
Basalt
Log [Conductivity (S/m)]
NBO/T
1.5
1.0
0.5
0.0
-0.5
-1.0
-1.5
-2.0
0.0
0.1
0.2
0.3
0.4
0.5
0.6
0.7
0.8
0.9
1.0

Figure 8

787 Table 1. Experimental conditions and results.

788

| Expt. no. | Sample | *P* (GPa) | *T* (K) | log$\sigma$ (S/m) | $\sigma_0$ (S/m) | $\Delta H$ (eV) | $\sigma_m$ (S/m) | Melt fraction (vol%) | Run products |
|---|---|---|---|---|---|---|---|---|---|
| R1040 | Amp25-Pl | 1.5 | 1300 | -1.41 | - | - | - | 6.7 | Grt-Cpx-Pl-quench Opx-melt |
| R1055 | Amp25-Pl | 1.5 | 1250 | -1.47 | - | - | - | 6.5 | Grt-Cpx-Pl-quench Opx-melt |
| R1056 | Amp25-Pl | 1.5 | 1200 | -1.51 | - | - | - | 5.9 | Grt-Cpx-Pl-quench Opx-melt |
| R1094 | Amp100 | 1.5 | 1300-950 | | 2663 | 0.85 | | 43.2* | Grt-Cpx-Quench Opx-melt |
| | | 1.5 | 900-600 | | 0.13 | 0.055 | | | |
| R1105 | Grt-Amp80 | 1.5 | 1300-1050 | | 3045.09 | 1.06 | 3.47 | 11.5* | Grt-Cpx-Quench Opx-melt |
| | | | 1050-700 | | | 0.50 | | | |
| R1106 | Grt-Amp60 | 1.5 | 1300-1100 | | 2421.03 | 1.05 | | 7.5* | Grt-Cpx-Quench Opx-melt |
| | | | 1100-800 | | 10.80 | 0.54 | | | |

789 *We counted the fraction of melts defined as melt[a] and melt[b] in table 3

790 Abbreviations: Amp, amphibole; Pl, plagioclase; Grt, garnet; Cpx, clinopyroxene; Opx,

791 orthopyroxene

792

793

794

795

796

797

798

799

800

801

802

803

804

805

806 Table 2. Major element compositions (wt%) of residual major minerals.

| | Amp | Grt | Amp | Cpx | Pl | Grt | | | | | | Pl | | |
|---|---|---|---|---|---|---|---|---|---|---|---|---|---|---|
| Run No. | Starting material (16LZWX2) | | Starting material (D17T87) | | | R1040 | R1055 | R1056 | R1094 | R1105 | R1106 | R1040 | R1055 | R1056 |
| N | 5 | 5 | 5 | 5 | 5 | 6 | 5 | 5 | 5 | 5 | 6 | 6 | 8 | 5 |
| SiO2 | 42.40 | 38.12 | 49.05 | 50.80 | 54.92 | 38.27 | 38.26 | 38.09 | 39.47 | 39.85 | 37.14 | 56.48 | 55.96 | 57.29 |
| TiO2 | 0.72 | 0.01 | 1.27 | 0.50 | 0.01 | 0.63 | 0.98 | 1.61 | 2.07 | 0.84 | 0.44 | 0.03 | 0.08 | 0.01 |
| Al2O3 | 14.93 | 20.61 | 6.54 | 3.21 | 27.73 | 20.55 | 20.41 | 19.97 | 19.90 | 19.76 | 20.84 | 27.66 | 26.75 | 26.86 |
| FeO | 16.33 | 28.02 | 12.55 | 11.87 | 0.21 | 24.99 | 24.19 | 22.40 | 21.21 | 22.06 | 26.05 | 0.31 | 0.36 | 0.33 |
| MnO | 0.00 | 2.00 | 0.12 | 0.33 | 0 | 0.53 | 0.48 | 0.43 | 0.37 | 1.02 | 3.06 | 0.01 | 0.01 | 0.00 |
| MgO | 10.35 | 4.10 | 15.05 | 12.96 | 0.01 | 6.25 | 6.19 | 6.35 | 8.45 | 7.45 | 4.46 | 0.02 | 0.17 | 0.02 |
| CaO | 9.00 | 5.20 | 11.17 | 20.87 | 10.52 | 7.62 | 7.72 | 8.85 | 8.31 | 7.43 | 6.37 | 8.75 | 9.64 | 8.97 |
| Na2O | 2.83 | 0.05 | 0.85 | 0.34 | 5.32 | 0.09 | 0.07 | 0.11 | 0.07 | 0.57 | 0.05 | 6.27 | 5.62 | 6.18 |
| K2O | 0.34 | 0.00 | 0.29 | 0.00 | 0.20 | 0.01 | 0.00 | 0.00 | 0.01 | 0.07 | 0.00 | 0.22 | 0.17 | 0.35 |
| Cr2O3 | 0.00 | 0.00 | 0.10 | 0.00 | 0.04 | 0.01 | 0.02 | 0.00 | 0.03 | 0.02 | 0.04 | 0.00 | 0.00 | 0.00 |
| Total | 96.90 | 98.11 | 96.99 | 100.88 | 98.96 | 98.94 | 98.32 | 97.83 | 99.89 | 99.07 | 98.45 | 99.75 | 98.77 | 100.01 |
| Total O= | 23 | 12 | 23 | 6 | 32 | 12 | 12 | 12 | 12 | 12 | 12 | 32 | 32 | 32 |
| Si | 6.33 | 3.06 | 7.15 | 1.90 | 10.00 | 3.01 | 3.01 | 3.01 | 3.02 | 3.09 | 2.98 | 10.17 | 10.19 | 10.29 |
| Ti | 0.08 | 0.00 | 0.14 | 0.01 | 0 | 0.04 | 0.06 | 0.10 | 0.12 | 0.05 | 0.03 | 0.00 | 0.01 | 0.00 |
| Al | 2.63 | 1.95 | 1.12 | 0.14 | 5.95 | 1.90 | 1.89 | 1.86 | 1.79 | 1.80 | 1.97 | 5.87 | 5.74 | 5.68 |
| Fe | 2.04 | 1.88 | 1.53 | 0.37 | 0.03 | 1.64 | 1.59 | 1.48 | 1.36 | 1.43 | 1.75 | 0.05 | 0.05 | 0.05 |
| Mn | 0.00 | 0.14 | 0.01 | 0.01 | 0 | 0.04 | 0.03 | 0.03 | 0.02 | 0.07 | 0.21 | 0.00 | 0.00 | 0.00 |

| | | | | | | | | | | | | | | |
|---|---|---|---|---|---|---|---|---|---|---|---|---|---|---|
| Mg | 2.31 | 0.49 | 3.27 | 0.72 | 0 | 0.73 | 0.73 | 0.75 | 0.96 | 0.86 | 0.53 | 0.00 | 0.05 | 0.00 |
| Ca | 1.44 | 0.45 | 1.75 | 0.84 | 2.05 | 0.64 | 0.65 | 0.75 | 0.68 | 0.62 | 0.55 | 1.69 | 1.88 | 1.73 |
| Na | 0.82 | 0.01 | 0.24 | 0.02 | 1.88 | 0.01 | 0.01 | 0.02 | 0.01 | 0.09 | 0.01 | 2.19 | 1.98 | 2.15 |
| K | 0.07 | 0.00 | 0.05 | 0.00 | 0.05 | 0.00 | 0.00 | 0.00 | 0.00 | 0.01 | 0.00 | 0.05 | 0.04 | 0.08 |
| Cr | 0.00 | 0.00 | 0.01 | 0.00 | 0.01 | 0.00 | 0.00 | 0.00 | 0.00 | 0.00 | 0.00 | 0.00 | 0.00 | 0.00 |
| Total | 15.71 | 7.97 | 15.29 | 4.00 | 19.98 | 8.01 | 7.98 | 7.98 | 7.97 | 8.01 | 8.02 | 20.02 | 19.94 | 19.98 |

807

808

809 Table 2/continued

| Minerals | Cpx | | | | | | Opx | | | | |
|---|---|---|---|---|---|---|---|---|---|---|---|
| Run No. | R1040 | R1055 | R1056 | R1094 | R1105 | R1106 | R1040 | R1055 | R1056 | R1094 | R1105 |
| *N* | 2 | 4 | 5 | 5 | 3 | 5 | 3 | 3 | 5 | 5 | 5 |
| $SiO_2$ | 51.07 | 51.39 | 51.73 | 45.78 | 50.61 | 49.25 | 51.24 | 51.45 | 51.82 | 51.46 | 52.07 |
| $TiO_2$ | 0.42 | 0.32 | 0.31 | 1.20 | 0.78 | 0.95 | 0.20 | 0.17 | 0.17 | 0.78 | 0.50 |
| $Al_2O_3$ | 3.15 | 1.42 | 1.54 | 10.84 | 6.91 | 5.51 | 0.64 | 0.65 | 0.69 | 4.72 | 6.46 |
| FeO | 10.88 | 8.97 | 9.04 | 15.81 | 13.79 | 14.75 | 21.93 | 21.38 | 21.72 | 15.40 | 15.85 |
| MnO | 0.38 | 0.41 | 0.42 | 0.17 | 0.20 | 0.36 | 0.87 | 0.80 | 0.87 | 0.23 | 0.59 |
| MgO | 14.82 | 13.64 | 13.64 | 11.63 | 12.53 | 12.47 | 20.86 | 21.50 | 21.40 | 23.26 | 20.03 |
| CaO | 16.75 | 21.88 | 21.60 | 11.05 | 13.39 | 13.31 | 0.92 | 0.94 | 0.87 | 2.50 | 2.93 |
| $Na_2O$ | 0.65 | 0.38 | 0.41 | 1.76 | 1.43 | 1.21 | 0.03 | 0.02 | 0.00 | 0.17 | 0.53 |
| $K_2O$ | 0.01 | 0.00 | 0.00 | 0.13 | 0.03 | 0.02 | 0.00 | 0.00 | 0.00 | 0.04 | 0.07 |
| $Cr_2O_3$ | 0.00 | 0.00 | 0.00 | 0.05 | 0.05 | 0.03 | 0.00 | 0.00 | 0.00 | 0.13 | 0.10 |
| Total | 98.14 | 98.41 | 98.70 | 98.42 | 99.73 | 97.86 | 96.69 | 96.92 | 97.56 | 98.69 | 99.13 |
| Total O | 6 | 6 | 6 | 6 | 6 | 6 | 6 | 6 | 6 | 6 | 6 |
| Si | 1.93 | 1.95 | 1.96 | 1.75 | 1.89 | 1.89 | 1.98 | 1.98 | 1.98 | 1.89 | 1.91 |
| Ti | 0.01 | 0.01 | 0.01 | 0.03 | 0.03 | 0.03 | 0.01 | 0.00 | 0.00 | 0.02 | 0.01 |
| Al | 0.14 | 0.06 | 0.07 | 0.49 | 0.30 | 0.25 | 0.03 | 0.03 | 0.03 | 0.20 | 0.28 |
| Fe | 0.34 | 0.29 | 0.29 | 0.51 | 0.43 | 0.47 | 0.71 | 0.69 | 0.69 | 0.47 | 0.49 |
| Mn | 0.01 | 0.01 | 0.01 | 0.01 | 0.01 | 0.01 | 0.03 | 0.03 | 0.03 | 0.01 | 0.02 |
| Mg | 0.84 | 0.77 | 0.77 | 0.66 | 0.70 | 0.71 | 1.20 | 1.23 | 1.22 | 1.27 | 1.09 |
| Ca | 0.68 | 0.89 | 0.88 | 0.45 | 0.54 | 0.55 | 0.04 | 0.04 | 0.04 | 0.10 | 0.12 |
| Na | 0.05 | 0.03 | 0.03 | 0.13 | 0.10 | 0.09 | 0.00 | 0.00 | 0.00 | 0.01 | 0.04 |
| K | 0.00 | 0.00 | 0.00 | 0.01 | 0.00 | 0.00 | 0.00 | 0.00 | 0.00 | 0.00 | 0.00 |
| Cr | 0.00 | 0.00 | 0.00 | 0.00 | 0.00 | 0.00 | 0.00 | 0.00 | 0.00 | 0.00 | 0.00 |
| Total | 4.01 | 4.02 | 4.01 | 4.04 | 4.00 | 4.00 | 4.00 | 4.00 | 4.00 | 3.99 | 3.96 |

810

811

812 Table 3. Chemical composition of the melts.

| Run No. | R1040 | R1055 | R1056 | R1094 | | | R1105 | | R1106 | |
|---|---|---|---|---|---|---|---|---|---|---|
| Sample | Amp25-Pl | | | Amp100 | | | Grt-Amp80 | | Grt-Amp60 | |
| Melt | Melt | Melt | Melt | Melt[a] | Melt[b] | Melt[c] | Melt[a] | Melt[c] | Melt[a] | Melt[c] |
| number | 5 | 5 | 7 | 5 | 5 | 5 | 5 | 5 | 5 | 5 |
| $SiO_2$ | 56.65 | 56.97 | 53.54 | 47.45 | 47.50 | 48.47 | 48.41 | 48.99 | 51.58 | 55.55 |
| $TiO_2$ | 0.92 | 1.33 | 1.09 | 2.69 | 2.85 | 2.97 | 1.54 | 2.03 | 1.28 | 2.31 |
| $Al_2O_3$ | 21.81 | 19.56 | 21.04 | 16.90 | 17.65 | 18.04 | 18.54 | 17.91 | 19.11 | 17.26 |
| FeO | 4.62 | 4.78 | 5.87 | 11.28 | 11.93 | 13.85 | 11.51 | 14.09 | 9.06 | 11.64 |
| MnO | 0.11 | 0.14 | 0.13 | 0.18 | 0.18 | 0.12 | 0.51 | 0.33 | 0.71 | 0.25 |
| MgO | 2.79 | 3.61 | 3.76 | 7.61 | 7.23 | 4.04 | 5.98 | 4.06 | 5.11 | 2.40 |
| CaO | 7.95 | 8.46 | 10.26 | 10.21 | 9.46 | 8.12 | 9.21 | 8.27 | 8.45 | 6.08 |
| $Na_2O$ | 4.71 | 4.71 | 3.84 | 3.19 | 2.76 | 3.19 | 3.78 | 3.56 | 4.10 | 3.35 |
| $K_2O$ | 0.42 | 0.44 | 0.47 | 0.45 | 0.43 | 1.20 | 0.50 | 0.76 | 0.59 | 1.16 |
| $Cr_2O_3$ | 0.00 | 0.00 | 0.01 | 0.03 | 0.02 | 0.01 | 0.02 | 0.00 | 0.00 | 0.00 |
| Total | 85.96 | 87.36 | 76.32 | 80.00 | 85.05 | 90.17 | 81.84 | 86.02 | 80.99 | 87.14 |
| $H_2O$[d] | 14.04 | 12.64 | 23.68 | 20.00 | 14.95 | 9.83 | 18.16 | 13.98 | 19.01 | 12.86 |

813 [a]Melt appears in the rim of the sample, in which no quench Opx occurs.

814 [b]Melt is separated from melt[a] by a clear boundary. Quench Opx coexists with melt[b].

815 [c]Melt coexists with Cpx and Grt.

816 [d]Water content is calculated as 100%-$c_{total}$. These values should be overestimated due to the
817 dissolved boron in the melt, which cannot be well quantitatively determined by EPMA. For
818 example, water content of melt of Amp100 sample can be roughly calculated to be 8.2 wt%, similar
819 to the water content (9.83 wt%) of melt[c], by the mass balance. Melt[c], far from the BN capsule and
820 showing the lowest water content, can better constrain the water content without boron
821 contaminations.

822